Supplemental Information for "Distinct methane-dependent biogeochemical regimes in Arctic seafloor gas hydrate mounds", Klasek et al.

Supplemental Figures

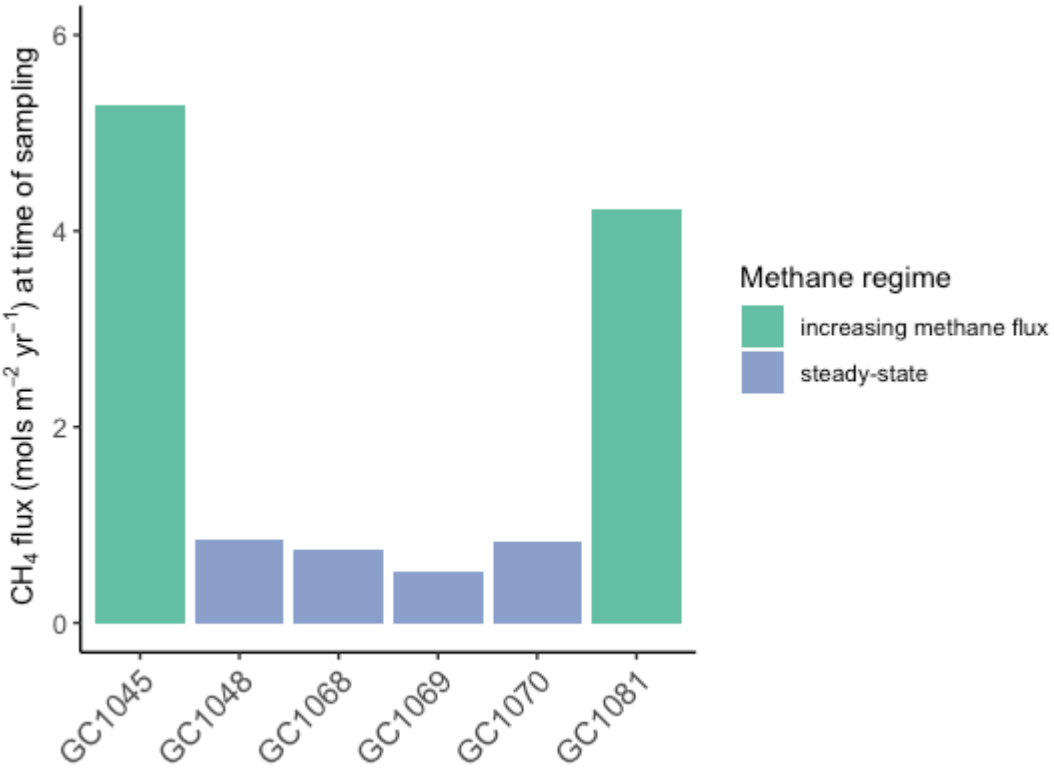

Figure S1. Methane fluxes at time of sampling for all gravity cores collected in this study. Fluxes are calculated by integrating rate measurements across the depth of cores. Assuming the drawdown in sulfate at PC1029 is associated with AOM only, we calculate a flux of 58.1 mols m^{-2} yr^{-1} at the site of active seepage, an order of magnitude higher than the two cores where methane flux is increasing.

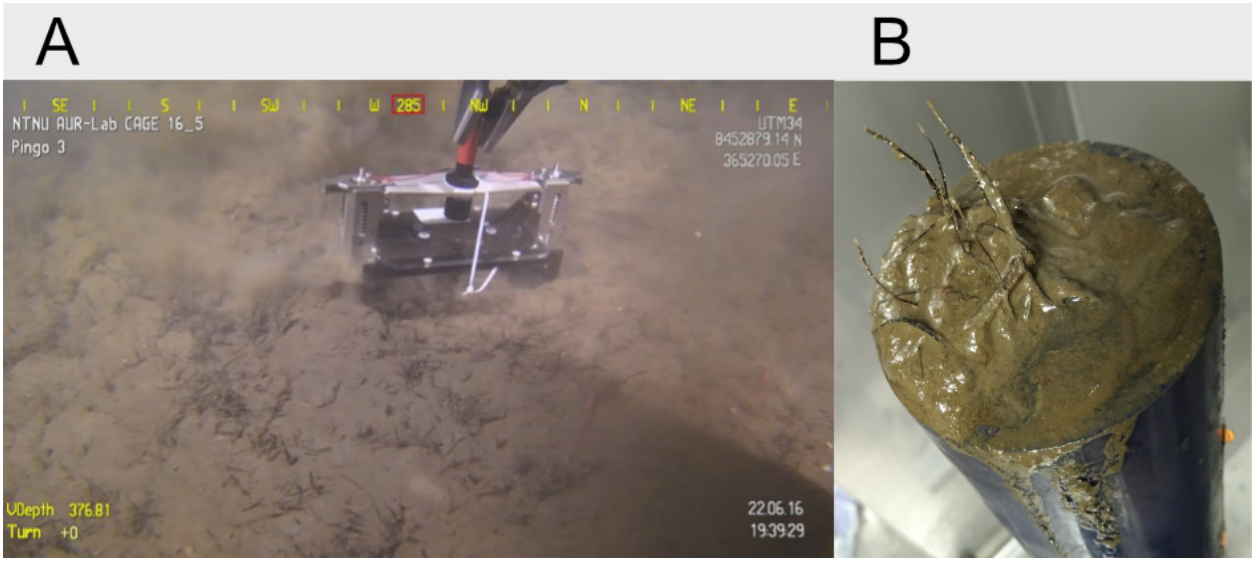

Figure S2. ROV image of Blade core (A) at the summit of GHM3 near where PC1029 was taken, showing abundant siboglinid tubes at the seafloor. An ROV-guided push core (replicate of PC1029) shows worm tubes in finer detail (B).

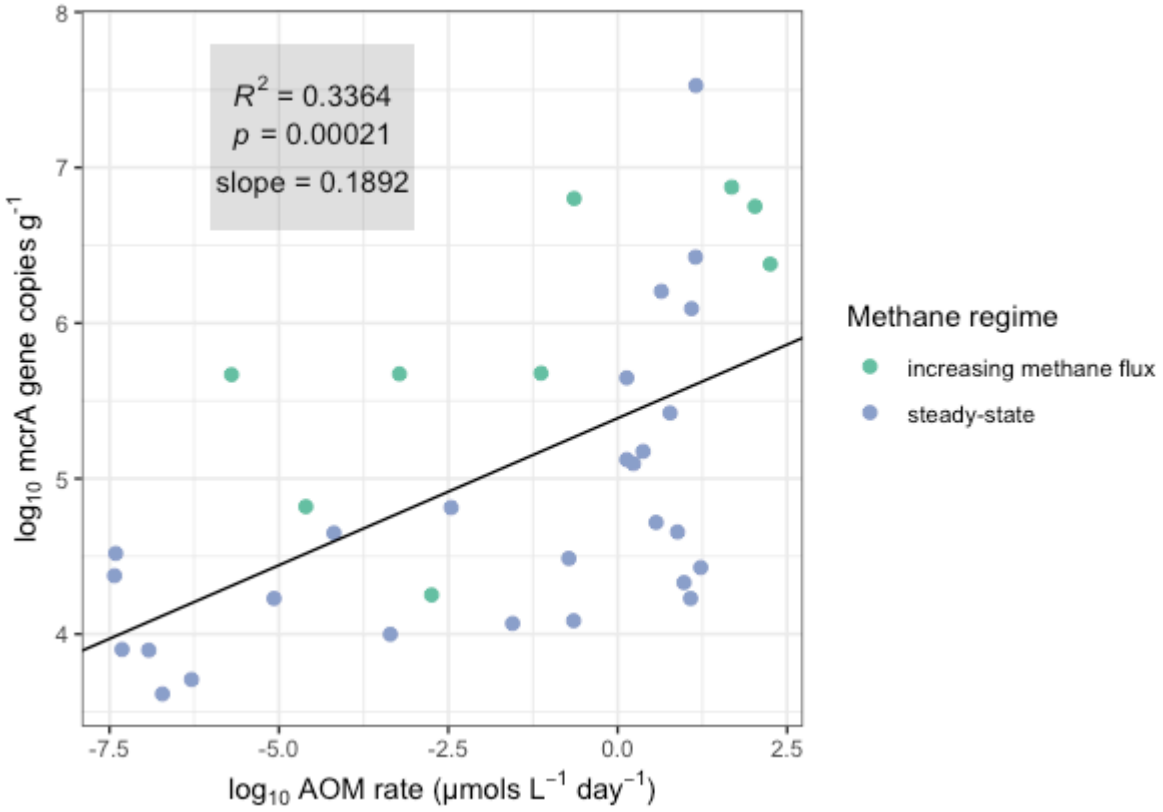

Figure S3. Regression of *mcrA* gene concentrations (copies per gram bulk sediment) to modeled AOM rates shows a positive relationship across samples from all cores (log-log transformation). Samples that did not contain detectable *mcrA* were not included. PC1029 samples were also

omitted due to uncertainties in calculating AOM rates.

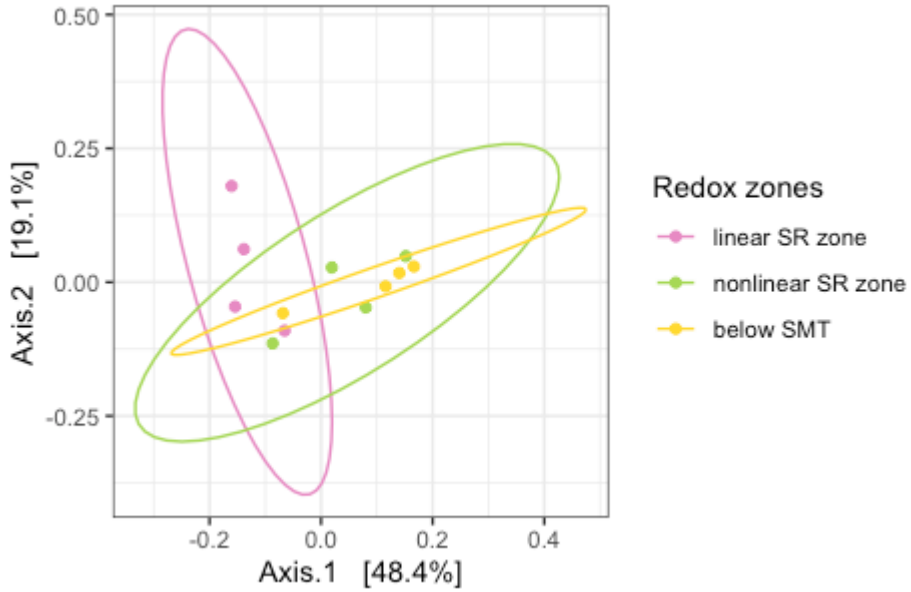

Figure S4. PCoA of communities from sites experiencing increasing methane flux suggesting linear SR zone communities are distinct from the other two zones. PERMANOVA test between linear and nonlinear, R^2 =0.30173, *p*=0.046; between linear and below-SMT, R^2 =0.42094, *p*=0.023; between nonlinear and below-SMT, R^2 =0.12485 *p*=0.435. A weighted Unifrac distance matrix with Hellinger transformation was used.

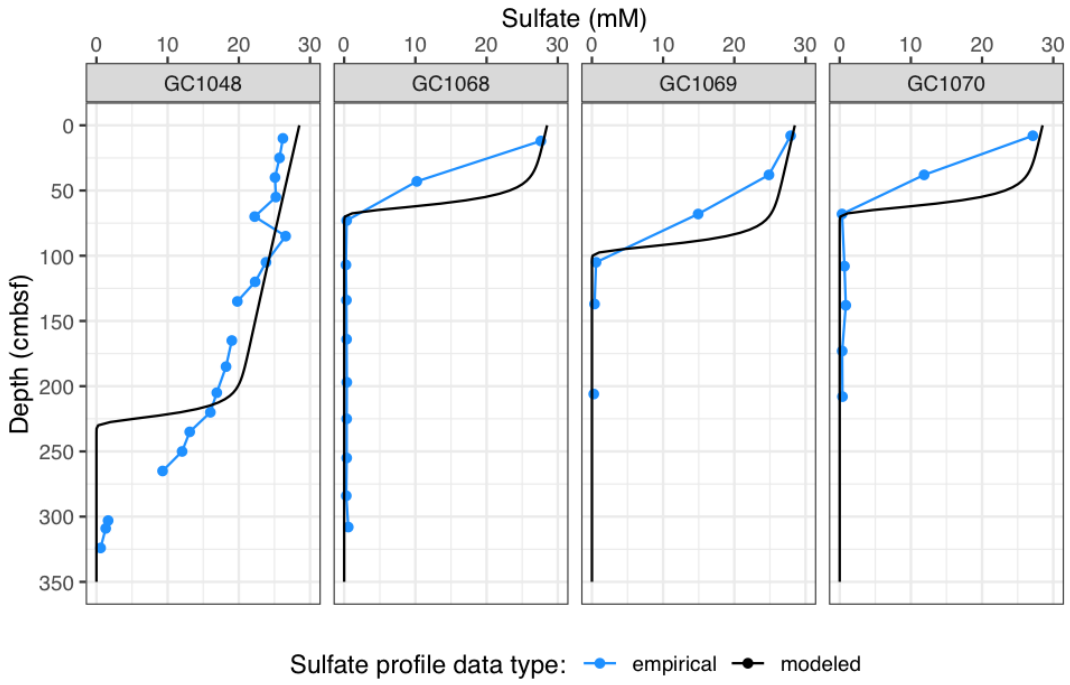

Figure S5. Empirically-measured sulfate porewater profiles from cores taken from steady-state areas, shown with modeled sulfate profiles if one were to assume a non-steady state scenario where methane flux was increasing. Discrepancies between these profiles justify our interpretation of these cores as steady-state.

Additional model justification

Two 1-D transport-reaction models to quantify AOM rates

We adopted two modeling approaches for the six gravity cores investigated from Storfjordrenna GHMs. For the two cores with concave upward porewater profiles (GC1045 and GC1081), we applied a model that only considers dissolved sulfate and methane to quantify the AOM rates under a non-steady state condition. For GC1048, GC1068, GC1069, and GC1070, we applied a model that accounts for additional porewater species and reactions to estimate AOM rates at these cores, which represent a steady state condition.

Non-steady state model for GC1045 and GC1081

The reduced model applied on these two cores[1] aims to quantify both AOM rates and the timing of SMT shoaling. The model considers a 60-m sediment column (the thickness of hydrate stability zone in the area) with the following assumptions:

(1) **AOM is the only reaction responsible for sulfate consumption at these sites.** The assumption is reasonable given the low concentration of ammonium measured. We measured up to ~200 μM of ammonium from the bottom of GC1045, which corresponds to 1.2 mmoles of organic carbon being degraded in every litter of porewater assuming a C/N atomic ratio of 6.1[2] (or 0.84 mmoles of organic carbon in very litter of bulk sediments). Such a small contribution of organic carbon degradation to sulfate reduction is negligible when estimating the rate of SMT shoaling.

(2) **The non-steady-state porewater profiles are the result of sudden increases in methane flux.** GC1045 and GC1081 lie in the vicinity of sites where non-steady-state porewater sulfate profiles were attributed to increasing methane flux[1], thus we see such an assumption is also applicable here. Briefly, Hong et al. examined the five different

scenarios that have been proposed in the literature that could cause similar non-steady-state porewater profiles[1]. Irrigation either due to biological or physical disturbance in the shallow sediments results in seawater-like pore water composition. The high ammonium concentrations measured in the shallow sediments (>58 μM from 10 to 54 cmbsf at GC1045) allow us to exclude this process. Irrigation enhances the mixing between oxic bottom water and pore fluid, and decreases the concentration of ammonium. Advection of the aqueous phase (i.e., pore fluid) is also excluded, as this process cannot explain the profiles from all solutes, such as calcium.

(3) **The sudden increase in methane supply is due to methane gas dissolution:** It was concluded that the high methane flux at GHM3 was due to methane gas dissolution[1,3], likely through the fracture network system in the region[3]. Presence of gas in the sediments was confirmed by the seismic blank zone beneath the investigated gas hydrate mound[3], gas hydrate recovered in the sediments, and the persistent hydroacoustic flare observed in the water column[3]. This interpretation was later supported by independent geophysical evidence[4].

In the model, only the aqueous phase was simulated. Both the AOM rates and timing are essentially constrained by the diffusion of sulfate and methane. The governing equations are:

Equation 1: $$\frac{\partial C}{\partial t} = -\frac{1}{\phi}\frac{\partial F}{\partial x} + R_{AOM}$$

Equation 2: $$F = -\phi Ds \frac{dC}{dx}$$

where φ, D_s, and $\frac{dC}{dx}$ are sediment porosity (0.7), diffusion coefficients in porous media, and concentration gradients for the two target species, t is time in years, x is depth in meters below seafloor (mbsf), C is the concentration of porewater species in mole/m^3 (volume of bulk sediments), and R_{AOM} is the AOM reaction rate in mole/m^3/yr. Diffusion coefficients for seawater media were corrected with bottom water temperature measured during CTD casts in May 2015 (0.56 ^{o}C) and a tortuosity of 1.5 to derive the diffusion coefficients in porous media

(D_s in Equation 2). We calculated 0.0072 and 0.0134 m^2/yr for the diffusion coefficients of sulfate and methane[5], respectively.

The simulation was done in two steps. In the first step, we derived the sulfate and methane profiles by progressing the model until sulfate profiles matched the shallow part of the profiles at each site by adjusting the methane concentration assigned at 60 mbsf as shown in Fig. S6. These derived profiles then served as the initial conditions for the second step of the modeling, where we increased the concentration of methane assigned at 60 mbsf to simulate the sudden increase of methane supply at these sites. For both steps, we assigned seawater composition as the top boundary condition and used no flux boundary as the lower boundary condition for sulfate. Rapid AOM stimulated by the high methane concentration consumes sulfate at rates that are much faster than the replenishing of sulfate through diffusion from the bottom water, resulting in the non-steady-state profiles observed. As the model does not include gas dissolution, AOM rates were constrained by the sulfate profiles. We calculated AOM numerically by discretizing depth using a centered forward finite difference scheme and time using an implicit Crank-Nicholson scheme. The depth and time discretization (*dx*=0.025 meter and *dt*=0.01 year) were determined by running the model with progressively smaller discretization until the results were numerically stable and accurate.

We solved the R_{AOM} term explicitly as:

Equation 3:
$$R_{AOM} = R_{AOM}^{\max} \frac{C_{SO_4}}{C_{SO_4} + k_{half-SO_4}} \frac{C_{CH_4}}{C_{CH_4} + k_{half-CH_4}}$$

Where $k_{half-SO_4}$ and $k_{half-CH_4}$ are the half saturation constants for sulfate[6] (0.5 mole/m^3) and methane[7,8] (5 mole/m^3), respectively. $R_{AOM}^{\max}$ is the theoretical maximum AOM rate which we obtained by fitting the sulfate profile (2 mol/m^3/yr). The magnitude of this value affects the shape of profiles close to the SMT depth, but not the rate of SMT migration.

There are two freely-adjusted parameters in this model: the lower boundary condition for methane (i.e., the concentration at 60 mbsf), and the time since the methane pulse initiated.

The first parameter was constrained both by the curvature of the sulfate profiles. The methane flux has to be great enough to simulate AOM that can outcompete sulfate diffusion from the seafloor. An insufficient methane flux will result in a sulfate profile that is smoother than the observed profiles[1]. With methane flux being constrained, we can estimate the duration of the methane pulse required to fit the data. The best fit results were shown in Fig. S7, with the AOM rate estimates shown in Figure 3B of the main text.

Steady state model for GC1048, GC1068, GC1069, and GC1070

For the other model, we applied a FORTRAN routine, CrunchFlow[9], to simulate sites with steady-state porewater profiles following the same setup as assigned before[10]. Detailed mathematical formulation of reactions can be found elsewhere[9]. We simulated sediment columns of 3 to 3.5 meters for 15000 years, the age of the sediment as determined previously[1]. We considered 11 primary porewater species (HCO_3^-, $CH_{4(aq)}$, NH_4^+, HPO_4^{2-}, HS^-, SO_4^{2-}, Fe^{2+}, Cl^-, Ca^{2+}, Mg^{2+}, and Na^+) and eight secondary species ($CO_{2(aq)}$, CO_3^{2-}, NH_3, H_3PO_4, $H_2PO_4^-$, PO_4^{3-}, $H_2S_{(aq)}$, and S^{2-}) to correctly account for the solution ionic strength and buffer capacity. Three reactions, organoclastic sulfate reduction (OSR), authigenic carbonate precipitation (CP), and sulfate reduction coupled to anaerobic oxidation of methane (SR-AOM) were included:

Equation 4 (OSR): $(CH_2O)(NH_3)_{0.169}(H_3PO_4)_{0.009} + 0.5\ SO_4^{2-} \rightarrow 0.348\ CO_2 + 0.652\ HCO_3^- + 0.348\ H_2O + 0.5\ HS^- + 0.169\ NH_4^+ + 0.009\ HPO_4^{2-}$

Equation 5 (CP): $Ca^{2+} + HCO_3^- \rightarrow CaCO_3 + H^+$

Equation 6 (SR-AOM): $SO_4^{2-} + CH_4 \rightarrow HS^- + HCO_3^{2-} + H_2O$

We assumed a constant porosity (0.7) throughout the core. Porosity was corrected for tortuosity by assigning a formation factor of 1.5. Diffusion coefficients for ions were computed[5] assuming a constant temperature of 0.56˚C based on the average seafloor temperature in the area[1]. Kinetic constants for all three reactions were derived based on the fitting of the observed porewater profiles (summarized in Table S3). For example, the kinetic constant for CP is

constrained by dissolved calcium profile; the constant for OSP is constrained by the profile of ammonium. We used the same kinetic constant as assigned previously[10] for SR-AOM. We assigned seawater composition to the upper boundary and initial conditions, and used a no flux lower boundary condition for all porewater species except methane. Methane was supplied to the sediment column through a source set (termed ME in Table S3) in the deepest cell (see Table S3 for the kinetic constants used). The slightly curved sulfate profile from core GC1048 may hint to a non-steady state condition similar to that for GC1045 and GC1081, but the observed biofilm[11] and deep SMT are evidence of a near-steady-state condition. We fitted the profiles by a similar two-step simulation with CrunchFlow to derive AOM rates at this site. This is done by initially fitting the shallow part of the profile (0-2.2 mbsf) and then increasing the bottom supply of methane in the next step of simulation. The best fit results of all cores were shown in Fig. S7.

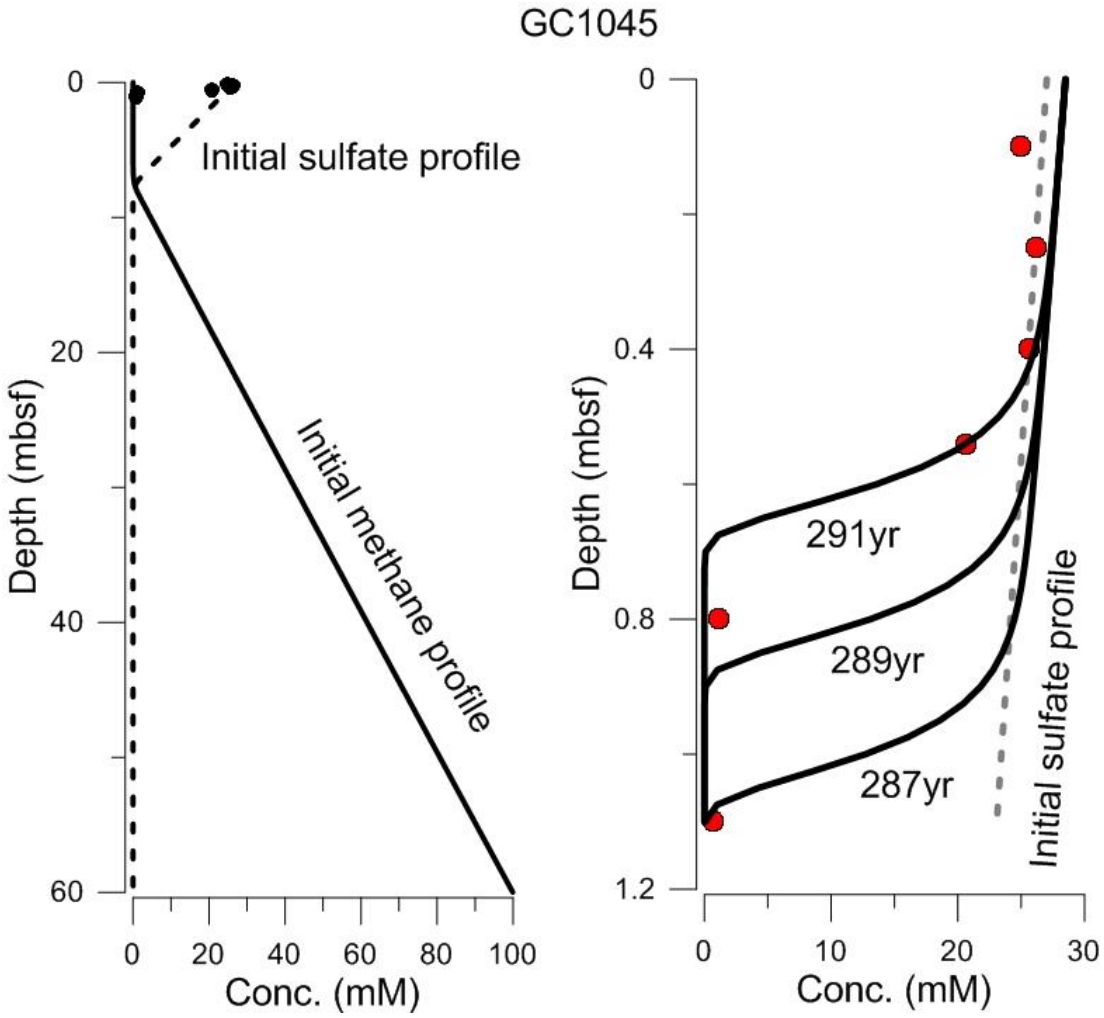

Figure S6. Initial condition and time progressing model results from the reduced numerical model applied on GC1045 and GC1081.

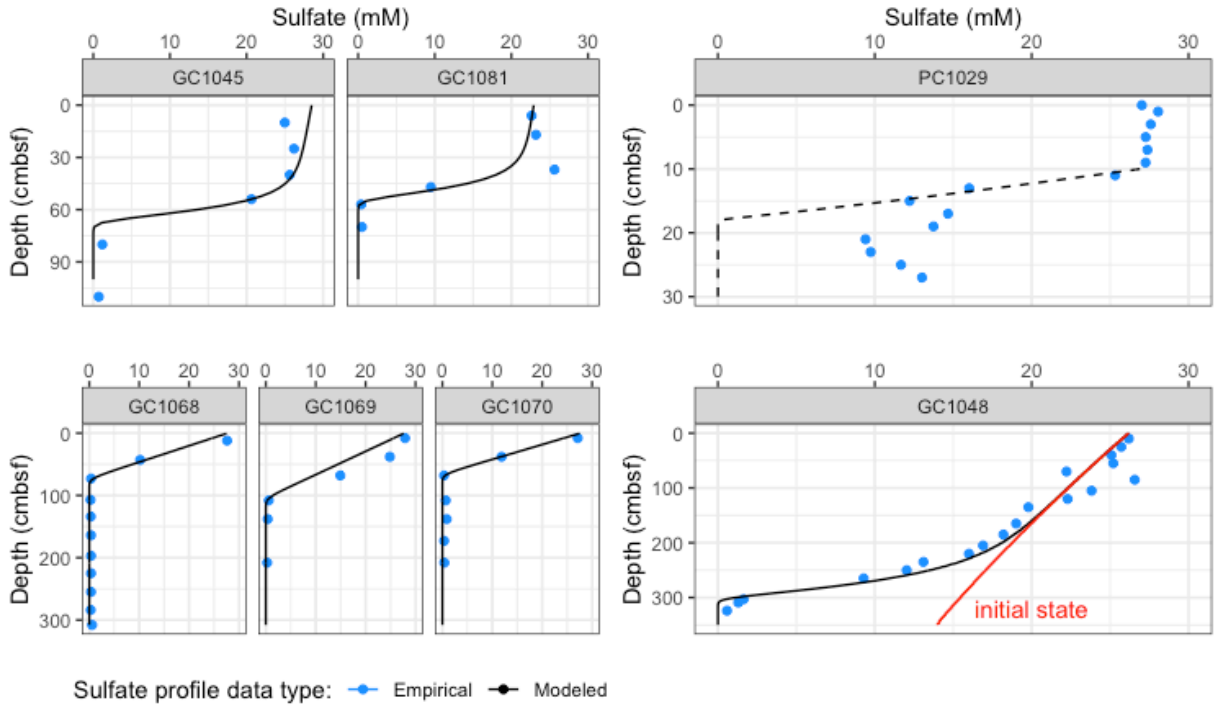

Figure S7. Porewater sulfate measurements from all cores in this study (blue dots) plotted alongside best-fit models (black lines). The inability to fit a model to sulfate measurements at PC1029 is demonstrated by a dashed line, while the red line in GC1048 represents an initial sulfate profile that fits the model.

Supplemental Tables

Core	Latitude	Longitude	Water depth (m)	Core recovery (cm)	SMT depth (cm)
PC1029	76 06.398	15 58.151	381	27	NA
GC1045	76 06.347	15 57.959	387	130	82
GC1081	76 07.022	16 02.593	369	102	56
GC1048	76 06.737	15 59.845	387	335	320
GC1068	76 06.739	16 00.311	384	295	108

GC1069	76 06.719	16 00.334	383	227	138
GC1070	76 06.703	16 00.162	385	326	69

Table S1. Latitude, longitude, water depth, core recovery, and sulfate-methane transition depth of all cores analyzed in this study.

(See Excel spreadsheet for Table S2)

Table S2. Increases in methane flux over the past two decades for cores GC1045 and GC1081 and corresponding depths of modeled peak AOM rates. Fluxes are integrated from AOM rate data, using cell widths of 2.5 cm. (Peak AOM depths also at 2.5 cm resolution).

	GC1048	**GC1068**	**GC1069**	**GC1070**
k-OSR	$\mathbf{10^{-9.5}}$	$\mathbf{10^{-10.5}}$	$\mathbf{10^{-10.5}}$	$\mathbf{10^{-10.5}}$
k-CP	$\mathbf{10^{-7.5}}$	$\mathbf{10^{-8}}$	$\mathbf{10^{-8.5}}$	$\mathbf{10^{-8.5}}$
k-ME	$\mathbf{10^{-6.5}}$	$\mathbf{10^{-5.6}}$	$\mathbf{10^{-5.9}}$	$\mathbf{10^{-5.5}}$

Table S3. Kinetic constant of the reactions considered (unit: $mol/m^2/sec$).

References

1. Hong, W.-L. *et al.* Seepage from an arctic shallow marine gas hydrate reservoir is insensitive to momentary ocean warming. *Nature Communications* **8**, 15745 (2017).
2. Tamelander, T., Aubert, A. & Wexels Riser, C. Export stoichiometry and contribution of copepod faecal pellets to vertical flux of particulate organic carbon, nitrogen and phosphorus. *Mar. Ecol. Prog. Ser.* **459**, 17–28 (2012).
3. Hong, W.-L. *et al.* Variations in Gas and Water Pulses at an Arctic Seep: Fluid Sources and Methane Transport. *Geophysical Research Letters* **45**, 4153–4162 (2018).
4. Waage, M. *et al.* Geological Controls on Fluid Flow and Gas Hydrate Pingo Development on the Barents Sea Margin. *Geochemistry, Geophysics, Geosystems* **20**, 630–650 (2019).

5. Boudreau, B. P. *Diagenetic Models and Their Implementation: Modelling Transport and Reactions in Aquatic Sediments*. (Springer Berlin Heidelberg, 1997).
6. Wegener, G. & Boetius, A. An experimental study on short-term changes in the anaerobic oxidation of methane in response to varying methane and sulfate fluxes. *Biogeosciences* **6**, 867–876 (2009).
7. Nauhaus, K., Boetius, A., Krüger, M. & Widdel, F. In vitro demonstration of anaerobic oxidation of methane coupled to sulphate reduction in sediment from a marine gas hydrate area. *Environmental Microbiology* **4**, 296–305 (2002).
8. Vavilin, V. A. Estimating changes of isotopic fractionation based on chemical kinetics and microbial dynamics during anaerobic methane oxidation: apparent zero- and first-order kinetics at high and low initial methane concentrations. *Antonie van Leeuwenhoek* **103**, 375–383 (2013).
9. Steefel, C. I. *et al.* Reactive transport codes for subsurface environmental simulation. *Comput Geosci* **19**, 445–478 (2015).
10. Hong, W.-L. *et al.* Removal of methane through hydrological, microbial, and geochemical processes in the shallow sediments of pockmarks along eastern Vestnesa Ridge (Svalbard). *Limnology and Oceanography* **61**, S324–S343 (2016).
11. Gründger, F. *et al.* Methane-fuelled biofilms predominantly composed of methanotrophic ANME-1 in Arctic gas hydrate-related sediments. *Scientific Reports* **9**, 9725 (2019).